INTERFACE

rsif.royalsocietypublishing.org

Research

Cite this article: Sherman VR, Yaraghi NA, Kisailus D, Meyers MA. 2016 Microstructural and geometric influences in the protective scales of *Atractosteus spatula*. *J. R. Soc. Interface* **13**: 20160595.
http://dx.doi.org/10.1098/rsif.2016.0595

Received: 28 July 2016
Accepted: 17 November 2016

Subject Category:
Life Sciences–Engineering interface

Subject Areas:
biomaterials, biomechanics

Keywords:
bioinspiration, armour, alligator gar, fish scales, hydroxyapatite, collagen

Author for correspondence:
Marc A. Meyers
e-mail: mameyers@ucsd.edu

THE ROYAL SOCIETY
PUBLISHING

Microstructural and geometric influences in the protective scales of *Atractosteus spatula*

Vincent R. Sherman[1], Nicholas A. Yaraghi[2], David Kisailus[2] and Marc A. Meyers[1]

[1]Materials Science and Engineering Program, University of California, San Diego, La Jolla, CA, USA
[2]Materials Science and Engineering Program, University of California, Riverside, Riverside, CA, USA

MAM, 0000-0003-1698-5396

Atractosteus spatula has been described as a living fossil (having existed for 100 Myr), retaining morphological characteristics of early ancestors such as the ability to breathe air and survive above water for hours. Its highly effective armour consists of ganoid scales. We analyse the protective function of the scales and identify key features which lead to their resistance to failure. Microstructural features include: a twisted cross-plied mineral arrangement that inhibits crack propagation in the external ganoine layer, mineral crystals that deflect cracks in the bony region in order to activate the strength of mineralized collagen fibrils, and saw-tooth ridges along the interface between the two scale layers which direct cracks away from the intrinsically weak interface. The macroscale geometry is additionally evaluated and it is shown that the scales retain full coverage in spite of minimal overlap between adjacent scales while conforming to physiologically required strain and maintaining flexibility via a process in which adjacent rows of scales slide and concurrently reorient.

1. Background

Scales have been a key form of protection for fish for hundreds of millions of years. Although most commonly found in fish and reptiles, scales may also be found in mammals: the pangolin is covered in keratinous scales [1]. Additionally, ancient Romans produced an armour named *lorica squamata*, in which individual iron or bronze scales were sewn to a fabric backing. Although it comes at an additional weight penalty in comparison with other armours, such as *lorica hamata* (chain mail), its effectiveness in battle made it an important defence for Roman legionnaires [2].

As implied by the name, the inspiration for the *lorica squamata* was likely drawn from a biological scale: squama means scales in Latin. Natural scales are becoming the subject of intense investigation [3–7] because of potential bioinspired applications. The most studied fish scales may be categorized into four types: placoid, cosmoid, ganoid and elasmoid. Placoid scales, which are commonly found on sharks, are denticles that feature a flattened rectangular base plate. They are embedded in the fish body and have spines that project from the posterior surface. Similar to teeth, these scales have a pulp core surrounded by a bone-like material (dentine) and an enamel-like outer layer (vitrodentine). Cosmoid scales likely evolved from the fusion of placoid scales, although a tissue complex known as cosmine takes the place of the pulpal core. Ganoid scales are rigid and jointed articulating scales consisting of a thin mineral surface layer made of hydroxyapatite, called ganoine, atop a bony foundation. Elasmoid scales evolved from the thinning of ganoid scales and consist of two subcategories: ctenoid and cycloid. Each consists of a bony mineralized surface layer and a fibrillary plate beneath, which is mostly collagen. Ctenoid scales have spines, which are bony growths distinct from the body of the scale, while the cycloid scales are smooth [8].

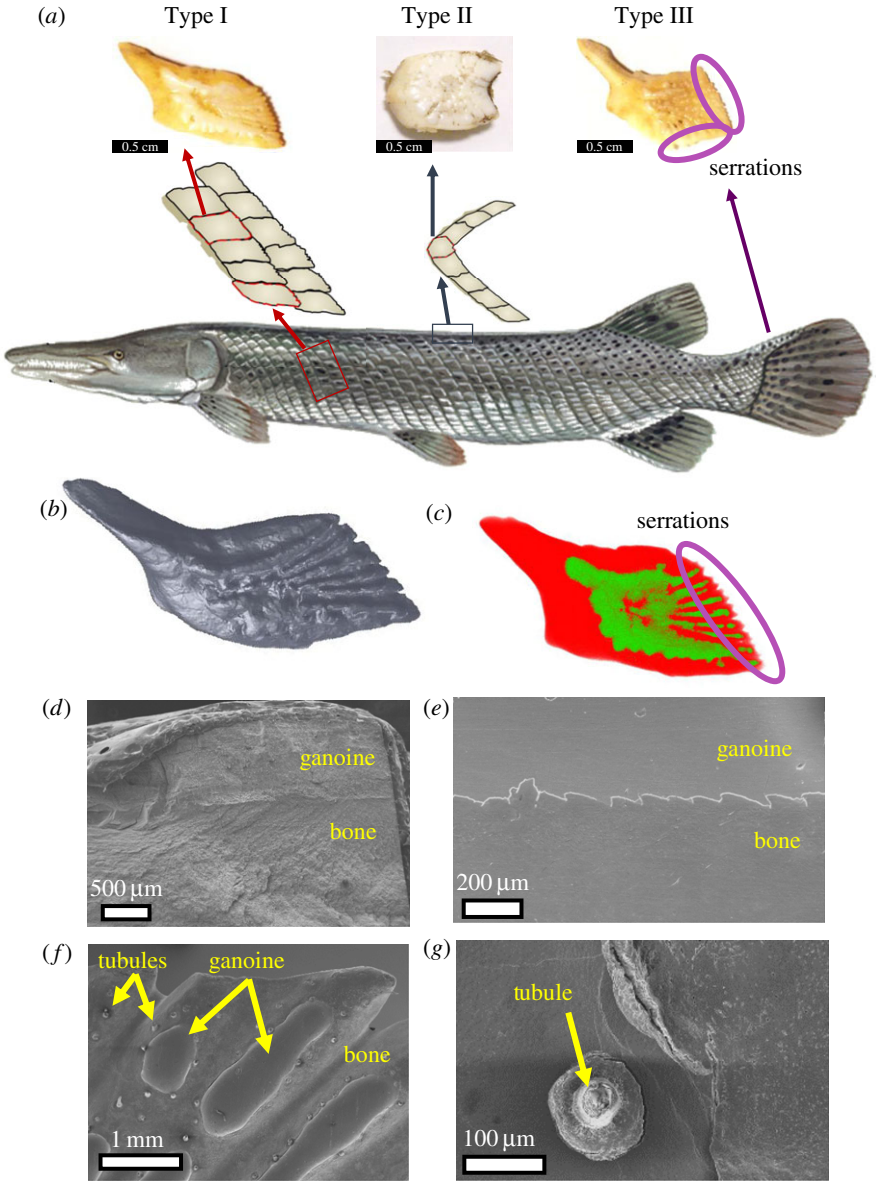

Figure 1. Hierarchical arrangement and features of an alligator gar scale. (*a*) Schematic shows the alligator gar and its three types of scales. Type I are the most common, covering the majority of the fish. Types II and III are found where Type I scales converge and on the edges of the fish. (*b*) Surface reconstruction from X-ray computed micro-tomography (µ-CT) of a Type I scale, revealing the morphology of the textured surface. (*c*) µ-CT where ganoine is shown in green and bone red. Ganoine does not completely cover the scale surface. (*d*) Scanning electron micrograph of fractured cross section of scale. The distinction between ganoine and bone is clear. (*e*) The saw-tooth interface between ganoine and bone observed in a polished scale's cross section. (*f*) The outer surface of the scale. Ganoine deposits are clearly visible. Tubules are visible in bone, but not in ganoine. (*g*) A tubule passes through the ganoine at the edge of the mineral; as additional mineral is deposited these tubules close. (Online version in colour.)

Bruet *et al*. [9] revealed materials design principles present in the penetration resistance of the ganoid scales of *Polypterus senegalus*, a small fish that reaches only approximately 200 g in mass and 20 cm in length. Its scales have multiple layers, each with unique properties, deformation mechanisms, and a specialized manner in which cracking and failure occur in order to absorb energy and protect the fish. Song *et al*. [3] demonstrated how the structure of the ganoid scale provides toughness, penetration resistance and non-catastrophic pathways for energy dissipation.

Atractosteus spatula, or alligator gar, is another fish with a ganoid-type scale and is the subject of our research. As one of the largest freshwater fish in North America, large gars may reach 140 kg in mass and 3 m in length. The fish, shown in figure 1, is characterized by a long cylindrical body covered in rigid articulating ganoid scales. Owing to attacks by other gars (self-predation) and alligators, the scales of this fish are required to perform exceptionally as an armour. Its scales resist the powerful ambush attack of its predators and interface in a way that allows the fish to maintain flexibility and motion in spite of the scales' individual rigidity.

While most modern fish have overlapping scales which are capable of bending as they swim, this is not the case for the gar or other ganoid fish. The stiff and inflexible design is optimized to protect against prehistoric and modern predators with powerful bite forces (e.g. up to 10 kN for the alligator) [10]. Large overlaps would prevent the stiff scales from being capable of motion, but some overlap is required to distribute forces applied to a single scale and reinforce the vulnerable junctions between them [11]. The impressive protection of the gar is well recognized; Chen *et al*. [12] revealed the stiffness and hardness of alligator gar scales, similar to those of *P. senegalus* [9], and Yang *et al*. [13] identified mechanisms which lead to their fracture resistance. Allison *et al*. [14] observed circumferential cracks (also observed on *P. senegalus*), which are hypothesized to be

beneficial by localizing fracture. However, certain important aspects of the scales have been overlooked. In this work, we describe previously unreported toughening features of the scale microstructure, and show how the scale's shape and arrangement on the fish optimizes a trade-off between protection and flexibility. These features are key to the effective protection of the alligator gar.

2. Material and methods

2.1. Scale acquisition

Arrays of scales were obtained from fish in southern Louisiana. They were dried and shipped to UC San Diego for testing.

2.2. Scanning electron microscopy

Hydrated scales were fractured by bending or by freeze fracturing. Some were polished through the cross section and etched using 15% phosphoric acid. All samples were coated with iridium prior to observation in a Phillips XL30 environmental scanning electron microscope.

2.3. Nanoindentation

Scales were mounted in epoxy and polished to produce a flat surface in two orientations: parallel and perpendicular to the scale surface. After hydration, hardness and reduced modulus mapping (5 s load, 2 s hold at approx. 3 mN load, 5 s unload) was performed in the ganoine region of both orientations. High load indents (5 s load to approx. 5 N peak load, 5 s unload) were applied to induce fracture.

2.4. Three-point bending tests

Scales were cut into specimens with approximately 8 mm width, 3 mm thickness and 20 mm length. They were hydrated and subjected to bending in an Instron 3367 equipped with a 30 kN load cell. A support span of 16 mm and a loading rate of 0.016 mm s^{-1} were applied.

2.5. Penetration tests

Hydrated scales were polished on the bottom to provide a flat surface. Some scales were polished on the top surface to remove the ganoine layer. Pressure was applied to the scales by a steel indenter with a tip angle of 60° and radius of approximately 300 μm. Additionally, an alligator tooth with a tip radius of 240 μm was pressed into an array of scales atop a rubber foam foundation. In both cases, the load was applied by an Instron 3367 equipped with a 30 kN load cell.

2.6. Simulations

Finite-element analysis was performed using COMSOL. A representative volume of 1.3 mm by 1.3 mm and 0.3 mm thickness with seven 6.5 μm tubules extending through the thickness was imported from Solidworks. Material properties were extracted from Yang *et al.* [13], and the dry gar scale was modelled as a linear elastic solid with a modulus of 1 GPa while the hydrated gar scale was modelled as a an isotropic elastoplastic solid with an elastic modulus of 1 GPa followed by a yield stress of 100 MPa and linear hardening with a tangent modulus of 266 MPa. A physics-controlled mesh of 58 342 tetrahedral elements was refined near the tubules in order to ensure an accurate solution. A tensile load of 70 MPa was applied as a step function to the top surface using a stationary solver, while the bottom surface was constrained to its initial plane.

2.7. X-ray microtomography

X-ray computed microtomography (μ-CT) was employed to visualize the three-dimensional morphologies of the gar scale by an Xradia 510 Versa scanner with a voxel size of 0.96 μm. Data were visualized using Amira software.

3. The hierarchical structure of alligator gar scales

The scales of the alligator gar have two distinct layers, clearly discernable in figure 1*a*. The white external layer consists of ganoine, which is hard and nearly pure mineral (hydroxyapatite), and covers 40–70% of the surface of the scale; this partial coverage is due to the overlap by surrounding scales as well as irregularities including ridges and gaps throughout. The foundation is a yellow bony composite of hydroxyapatite and collagen. Three types of scales are required to effectively cover the alligator gar surface, characterized by shape. Figure 1*a* shows the three scales in the orientation in which they appear on the fish: Type I scales have an approximately rhombic shape and one serrated edge pointed towards the back of the fish. They overlap in a regular pattern forming inclined rows on most of the fish. It is theorized that the serrated edge may slice the skin of the predator and act as a form of defence as the fish thrashes. The aspect ratio (thickness to length) is 7.8 ± 0.9 and the degree of imbrication (length exposed to total length of scale) is 0.75 ± 0.04. Thus, the scales are thick and have minimal overlap as compared to other fish scales. A μ-CT reconstruction of the morphology of Type I scales is shown in figure 1*b*,*c*, with the mineral-dense ganoine shown in green, and the bony foundation in red. Type II scales form the dorsal ridge, where rows of Type I scales from the two sides converge. Type III scales are the least common; they have two serrated edges and occur in the dorsal tail of the fish.

3.1. Microstructure of scales

Figure 1*d* shows the fracture surface through the thickness of a Type I scale; the interface between the ganoine and bone is clearly distinguishable. Similarly, figure 1*e* shows a polished cross section of the Type I scale; the two layers are separated by a saw-tooth shaped interface. Figure 1*f* shows the external surface of the Type III scale near the serrated edge, where bone remains exposed and some tubules are observed at the surface. These tubules are covered by ganoine as it grows, a process which continues throughout the gar's life. Prior to being fully covered, a crater-like pit forms around the tubule; a tubule in the process of being covered by mineral is shown in figure 1*g*. It is also important to note that ganoine is a true enamel, meaning a layer of skin covers the entire surface of the scales and continuously deposits mineral in the living fish.

The microstructures of all scale types are comparable. The ganoine has a structure which consists of regular and distinguishable layers of hydroxyapatite mineral; each layer is approximately 30 μm in thickness and consists of sub-layers of 2–3 μm. Layers are made of bundles of twisted cross-plied mineral oriented, on average, approximately normal to the scale surface. These layers are shown in figure 2*a*, and a close-up of one layer is shown in figure 2*b*. This is different from some other ganoid scales; in *P. senegalus*, for example, the ganoine consists of parallel mineral fibres oriented directly

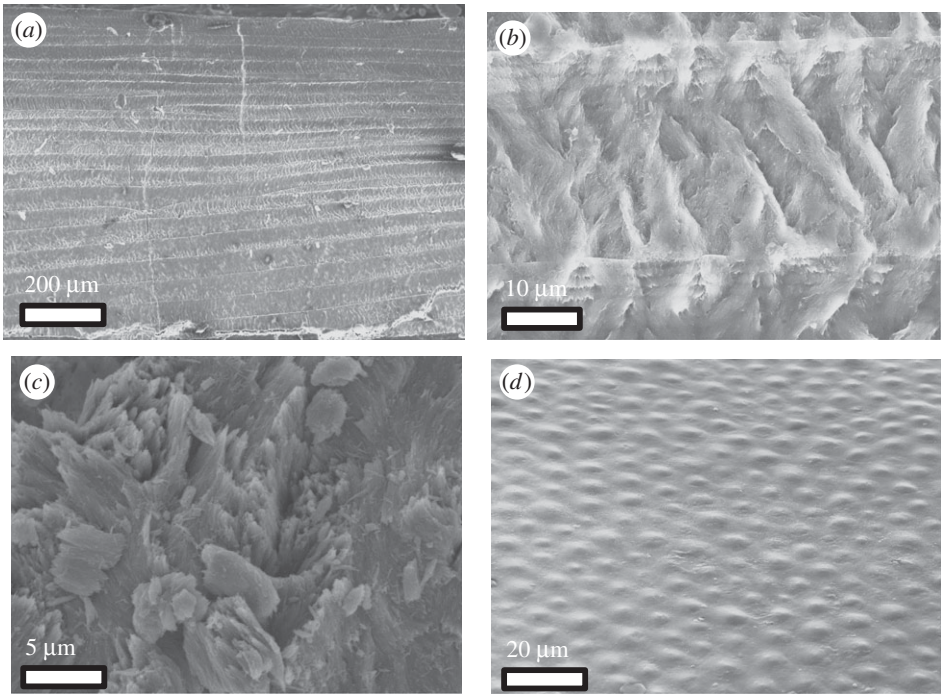

Figure 2. Structure of ganoine layer of the scale. (*a*) Etched ganoine cross section reveals mineral layers of approximately 30 µm thickness. (*b*) High magnification of a ganoine layer shows crossed mineral bundles, and sub-layers of 2–3 µm thickness. Bundles are oriented near perpendicular to the surface of the scale. (*c*) A fracture surface of the ganoine viewed from above the scale shows protruding mineral crystals. (*d*) The exterior surface of ganoine has tubercles (small rounded reliefs), which correspond to the heads of the mineral bundles.

towards the scale surface [9]. This may be due to the widely different thicknesses (*P. senegalus*: 10 µm versus *A. spatula*: 600 µm) of the ganoine layers. Figure 2*c* shows a fracture surface where mineral crystals protrude from the page, showing that they are oriented normal to the surface of the scale. Figure 2*d* is the external surface of the ganoine, where small protrusions called tubercles [15] are regularly arranged at approximately 7 µm across the surface of the scale. This spacing matches the periodicity and corresponds to the heads of the mineral bundles, and tubercles result from the speed of mineral deposition [16].

The bone of the scale consists of mineralized collagen fibrils normal to the scale surface, embedded in a mineral matrix. These fibrils are visible in figure 3*a*, where mineral crystals fill the space between fibrils (close-up shown in figure 3*b*). Figure 3*c* is a high-resolution view of a collagen fibril, where the mineral has nucleated in the intrafibrillar region of the collagen fibril. Mineralized fibrils are desirable because their toughness far exceeds that of the hydroxyapatite and collagen constituents, as shown by Buehler [17]. Hollow tubules run parallel to the fibrils throughout the thickness of the scale. Also shown in figure 1*f*, these tubules are clearly visible in figure 3*d*, which is a polished section of the scale as viewed from the normal direction, and visualized using µ-CT in figure 3*e*. These tubules are vascular channels that deliver nutrients to the skin covering the scales, but have also been attributed to toughening the dry scale [13].

3.2. Arrangement of scales and flexibility

The macroscopic arrangement of the scales is key to their effectiveness, allowing stiff and strong individual scales, reinforced with the crafted microstructures, to flex and conform to the fish's body as it swims without sacrificing complete protective coverage. It also enables a redistribution of stresses from the point of application due to a tooth over a broader area.

In order to compensate for their rigidity, the scales are arranged in such a way that allows geometric flexibility—this is what enables the fish to move as it swims. This is illustrated in figure 4*a*: adjacent scales have matching radii of curvature at their interfaces, which allows for a hinge-like motion on one another as they slide. An array of scales can be bent both towards and away from the surface, forming convex and concave surfaces, respectively, while maintaining full coverage, as is shown in figure 4*b*,*c*. Figure 4 shows scales at the maximum deflections; in their natural configuration, each scale may form an angle of approximately 6° with the adjacent scales. This limit is due to the extensibility in the soft tissues, which connect adjacent scales. The amount of curvature possible is dictated by the misorientation between adjacent scales and the total number of scales. Therefore, scales must be sufficiently small to achieve high amounts of curvature on the fish body. Figure 4*d* shows how deflection (measured by Δ) is a function of the ratio of scale length (l) to total fish length (L) and misorientation between scales (α). Figure 4*e* plots Δ as a function of α, l and L, based on the relationship [18]

$$\frac{\Delta}{L} = \frac{1}{\alpha}\left[1 - \cos\left(\frac{\alpha L}{2l}\right)\right]. \tag{3.1}$$

During this rotational deflection, the matching curvature of adjacent scales maintains full protective coverage without the formation of gaps. It is also important that the scales do not separate from their foundation during curvature. This effect is shown in figure 5*a*, and δ, the gap between scales, may be calculated as a function of scale length (l) and

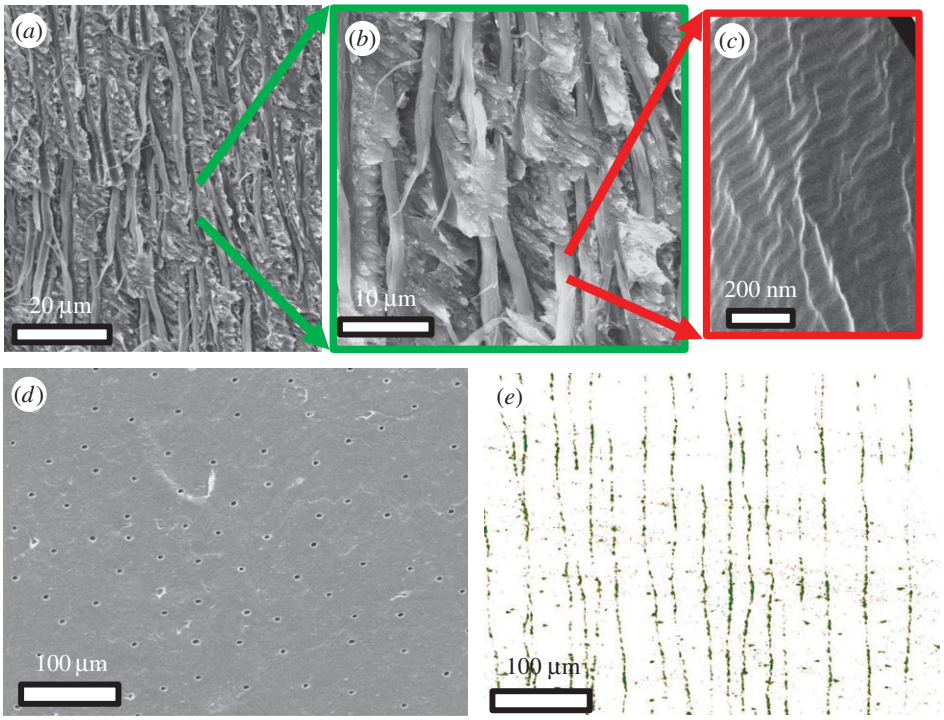

Figure 3. Structure of the bony layer of the scale. (*a*) Fractured surface of bone reveals parallel collagen fibrils. The space between the fibrils is filled with mineral crystals. (*b*) Increased magnification shows that the mineral crystals are oriented across the collagen fibrils. (*c*) High-resolution image of a mineralized collagen fibril. Mineral nucleates in the gap region of collagen fibrils, and the 67 nm banding is retained as mineral crystals grow. The mineralized surface of the fibril is characterized by flat surfaces and characteristic angles, which reduce the surface energy of the mineral. (*d*) Scanning electron micrograph of polished section of the bony region of scale. Vascular channels called tubules are numerous. (*e*) µ-CT reconstruction shows that tubules are parallel to each other and nearly perpendicular to the scale surface. They run from the base of the scale towards the outer ganoine surface, where they terminate. (Online version in colour.)

bending radius (R) through the relationship

$$\frac{\delta}{l} = \frac{1}{\sin(\arctan(l/R))} - \frac{R}{l}. \tag{3.2}$$

As the normalized ratio of R/l decreases, the size of gaps (δ/l) increases. The relationship between these parameters is plotted in figure 5*b*.

Simple flexing of scale arrays is not sufficient. An additional requirement is the ability to conform to a change in length of approximately 25%, which is both positive on the outside surface and negative on the inside, as calculated through measurements of a highly flexed fish. This dimensionless value is determined from photographs of gars using a simplified representation, shown in figure 6*a*. The body of the fish is modelled as a cylinder, and the maximum strain based on thickness ($2r$), bending radius (R) and degree of flexing (θ) is

$$\varepsilon_{\max} = \frac{\text{final length}}{\text{initial length}} - 1 = \frac{(R+r)\theta}{R\theta} - 1 = \frac{r}{R}. \tag{3.3}$$

Linear sliding between scales cannot accommodate this large strain due to the small percentage of overlap between them. Thus, the scales must both slide and reorient in a specialized and biomechanically optimal manner that can be decomposed into the three stages shown in figure 6*b*,*c*: increase in length shown by d, which produces tensile extension but leads to separation between scales; sliding shown by s, which is a vertical shift and closes the gaps; and lastly, a rotation of the scale array of β. These three components are permitted by the compliance of the connective tissue between the gar scales and enable the scale arrays to accommodate the significant dimensional changes required by the movement of the fish. The minor angle of the scales (γ) has a significant effect on the requirements of the scales to rearrange and provide protection. There is a trade-off between protection and physiological requirements: a minimal amount of weak interfaces is optimized as γ approaches 90°, but the physiological requirement of maintaining coverage causes a large amount of sliding (s) to close the separation (d) as γ approaches 90°, while reorientation of the scale array becomes excessively large. With respect to s and d, γ must be sufficiently small in order to be mechanically feasible. This relationship is

$$\frac{s}{d} = \tan\gamma. \tag{3.4}$$

It is also desirable to maximize the individual scale coverage, hence minimizing the length of perimeters that create interfaces, which are weaker regions. The reduction in coverage for a scale of a certain perimeter based on γ is

$$\frac{A_{\max}}{A} = \frac{l^2}{l^2\sin\gamma} = \frac{1}{\sin\gamma}, \tag{3.5}$$

where A is the area of a scale and l is the length of one side of the scale. Equations (3.4) and (3.5) are plotted in figure 6*d*. As γ approaches 0 (elongated scales), minimal s/d ratios result, but there is a large reduction in scale area compared to a square scale of the same perimeter. As γ approaches 90°, a nearly square scale optimizes the coverage but leads to infeasible ratios of s/d and excessive reorientation required of the scale arrays. The rotation of the scales, β, is equal to

$$\beta = \tan^{-1}\left(\frac{s}{d+l}\right) = \tan^{-1}\left(\frac{d\tan\gamma}{d+l}\right). \tag{3.6}$$

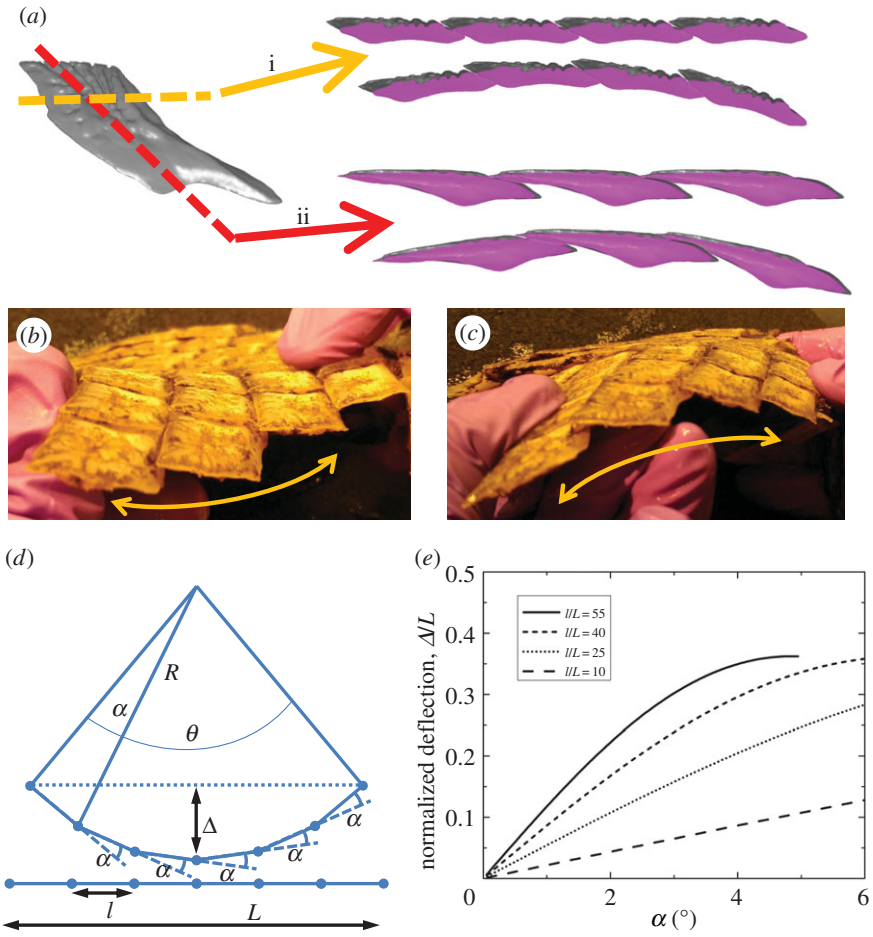

Figure 4. Geometric flexibility for a stiff scale. (*a*) Each scale has two directions of overlap; a cut in each direction is shown by the dashed lines. Overlapping scales hinge on adjacent edges with similar radii of curvature, as shown in the μ-CT cross sections. Most movement required due to the swimming of the fish is achieved by the motion shown in (i). (*b*) Scale array bending to create a concave surface. (*c*) Scale array bending to create a convex surface. (*d*) Manner in which scales on fish accommodate the deflection of the fish body (Δ). (*e*) Maximum normalized deflection (Δ/*L*) as a function of α for different ratios of scale length to fish length (*l*/*L*); adapted from Chen *et al*. [18]. (Online version in colour.)

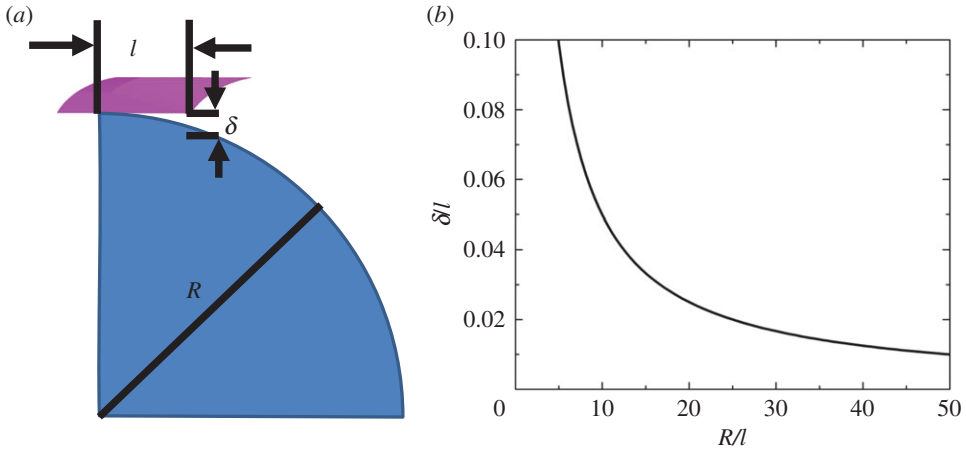

Figure 5. Relationship between scale size, separation and radius of bending curvature. (*a*) Schematic shows the unavoidable separation (δ) between flat scales of length (*l*) on a curved surface with radius of curvature (*R*); (*b*) relationship between *R*, *l* and δ. (Online version in colour.)

The optimal value of γ lies somewhere between; a physiological value is found by measuring scales, equal to 55°. This value is marked on the plot. A well-designed scale captures effectiveness in coverage and allows for the flexibility of the natural armour. Both size (*l*) and shape (γ) are important.

4. Mechanical performance of the gar scale

The mechanical performance of gar scales is summarized in figure 7*a* [12–14,19]; the solid lines show the compression results of approximately 2 mm hydrated cubes cut from the bony region of gar scales [13]; characteristic responses are

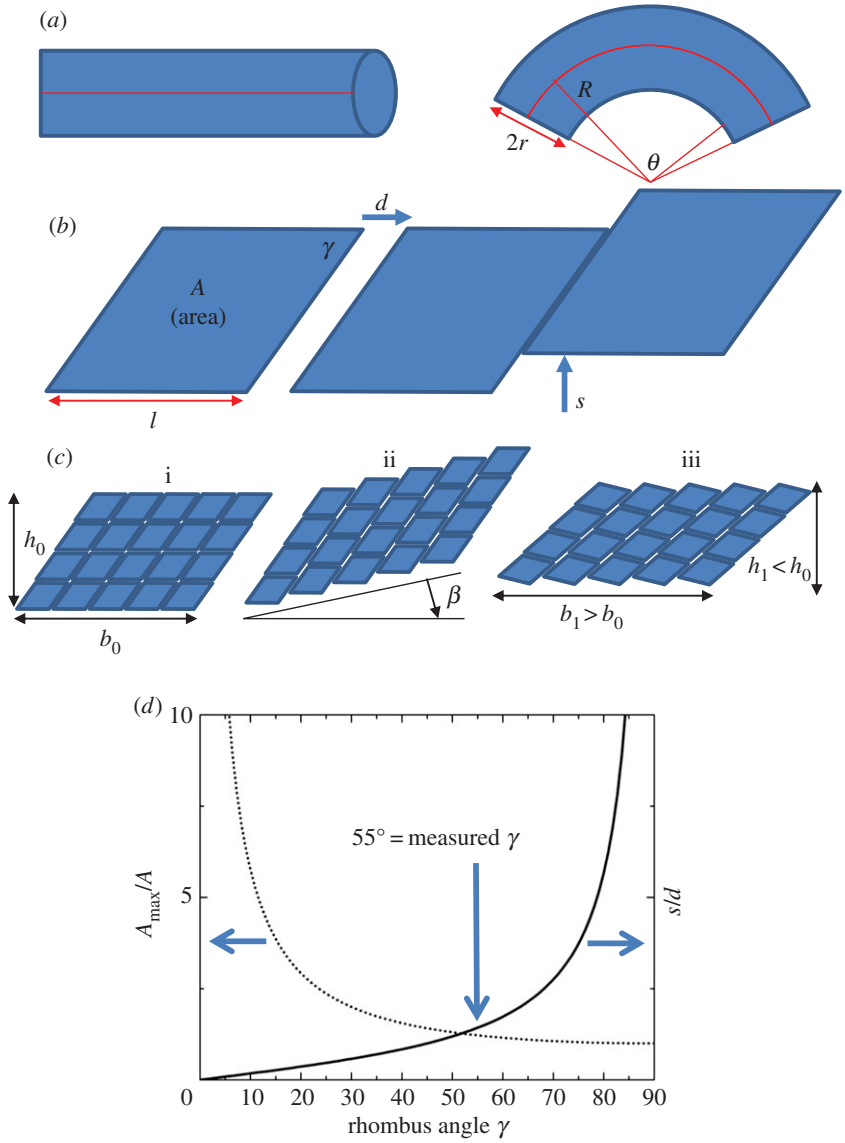

Figure 6. The mechanics of gar scales flexing. (*a*) A simple model of the gar's flexing, which is used to calculate the maximum strain that must be accommodated by the gar scales. (*b*) Translation by the scale to accommodate strain: *d* is extension, which lengthens the array but leaves gaps. *s* is shift, which closes the gaps formed by *d*. (*c*) (i) The original array of scales, (ii) translation by *d*, *s* and (iii) rotation of β, which results in the accommodation of strain ($b_1 > b_0$). (*d*) Ratios that effect the scale coverage area (A_{max}/A) and amount of sliding required (s/d) as a function of γ; it is desired that both are minimized; 55° is measured from fish as the value of γ. (Online version in colour.)

shown in black (compressed normal to the scale surface) and green (compressed in orthogonal directions parallel to the scale surface). The compressive strength and failure strain of hydrated samples vary widely: perpendicular to the surface respective values are 310 ± 30 MPa and approximately 0.3, and in the two in-plane directions strengths are 200 ± 30 and 240 ± 30 MPa with strains of approximately 0.17 and 0.25. By contrast, the moduli reported by nanoindentation vary by less than 1% when wet (9.98–10.04 GPa) and roughly 25% (10.9–13.8 GPa) when dry [13]. There are two key findings in these results. Firstly, in-plane mechanical properties of the scale do not have significant anisotropy due to the reported uncertainties. This is reasonable as there are no apparent structural features that would lead to in-plane anisotropy. Secondly, the ultimate strength and failure strain normal to the scale surface under compression are significantly improved from the two in-plane directions. This is due to microstructural features including the presence of collagen fibrils and tubules, which enhance the failure properties, and are discussed thoroughly in §5. However, these differences are not manifested during nanoindentation, which evaluates small material regions without tubules and does not induce failure.

Figure 7*a* also shows band plots of tensile curves from tests performed in-plane with the surface of the scale and highlight differences between the wet and dry responses [13]. Both exhibit similar stiffness and strength, but there is a notable and important difference: wet scales experience plasticity in tension, which is due to the breaking and reforming of hydrogen bonds between water molecules and collagen fibrils. This occurs when a critical stress is reached and hydrogen bonds within the scale no longer support the load. Upon unloading, the plastic strain, which is the strain after the transition, is not recovered. We find that this bilinear response plays a crucial role in the failure aversion of the gar scale and discuss this in §5. Dry scales, on the other hand, fail with less nonlinear deformation. Figure 7*b* shows the variation in microindentation and nanoindentation hardness throughout the (normalized) thickness of the scale [20]. Owing to distinct differences in the structure and

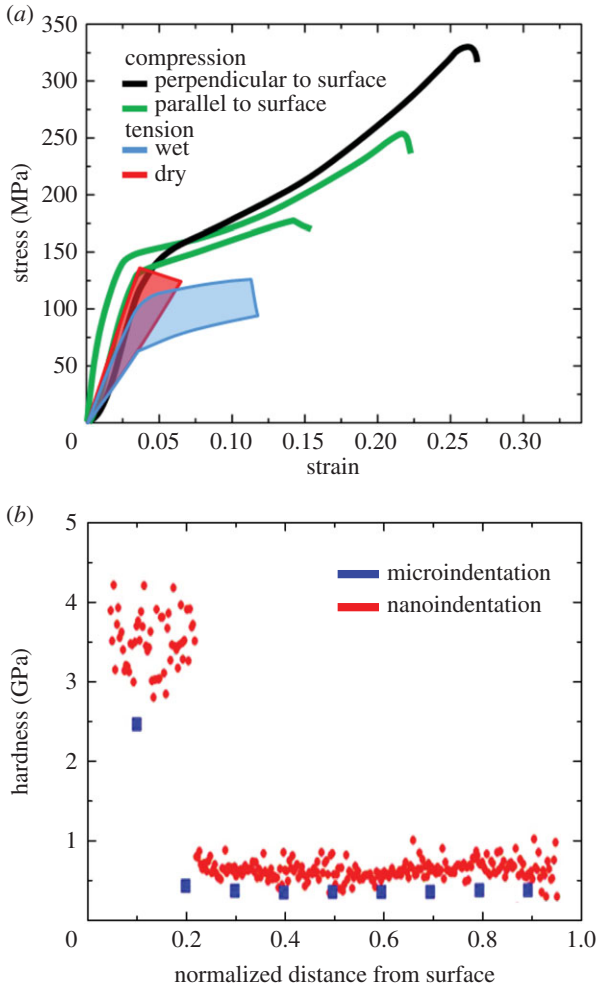

Figure 7. Previously reported mechanical properties of the scale. (*a*) Compressive tests of approximately 2 mm cubes in multiple orientations and range of tensile stress–strain curves of wet and dry alligator gar scales tested along the length of the scale. Note the bilinear response of the wet gar scale. Adapted from Yang *et al.* [13]. (*b*) Hardness of the scale. The ganoine outer surface is roughly six times harder than the bony part of the scale. There is little variation within each individual region. Adapted from Chen *et al.* [12]. (Online version in colour.)

composition of the ganoine and bony regions, an abrupt change (characteristic of ganoid scales [10]) occurs at the interface between the two. The higher microindentation hardness is in ganoine (2500 MPa) and the lower in the bony region (approx. 350 MPa) [12].

The ganoine exhibits structural anisotropy, shown in figure 3, where twisted cross-plied bundles of mineral extend towards the surface of the scale. Nanoindentation was performed and loading was applied in two orientations: inclined to the scale surface (nearly perpendicular to it), and parallel to the scale surface. The slightly inclined orientation was chosen so that mappings would span the approximately 30 µm thick cross-plied mineral layers, and show corresponding variation in properties. Results indicate that the ganoine is indeed anisotropic: when loaded in the direction aligned with the plane of the scale, the reduced modulus (E_r) is 59 ± 6 GPa. In the direction nearly perpendicular to the scale surface, the stiffness is increased ($E_r = 67 \pm 5$ GPa). These indentations are shown in figure 8*a*, with the interface between layers marked. Figure 8*b* shows the gradient in stiffness across the mineral layer, which is observable in both orientations; these gradients also result in increased uncertainties. The differences within layers correspond to the structure and organization of the mineral bundles in each layer, which also contribute to the toughening of the mineral. High load indents (figure 8*c*,*d*) show areas where failure was induced. The fracture toughness of the two orientations may be estimated [21,22]:

$$K_c = A\left(\frac{E}{H}\right)^{0.5}\frac{P}{c^{3/2}}, \tag{4.1}$$

where E is the Young's modulus, H is the hardness, P is the load, c is the half-crack length (measured from the centre of the indent to the crack tip) and A is a fitting parameter equal to 0.04 [23]. Although this technique is designed for isotropic and homogeneous materials, it has been applied for anisotropic and inhomogeneous materials such as enamel or ceramic coatings where conventional toughness tests are not feasible [24]. The maximum crack size from 5 N indents perpendicular to the scale surface is approximately 60 µm, while the maximum crack size from 5 N indents parallel to the surface is approximately 140 µm; the corresponding fracture toughness estimates are 2.8 and 0.8 MPa $m^{1/2}$, which compare well with tooth enamel ($K_c = 0.7$–1.27 MPa $m^{1/2}$). This fracture toughness is superior to that of single crystal hydroxyapatite, and indicates that the ganoine is toughened by the cross-plied mineral bundles, which are observable throughout. Additionally, the ganoine is 3.5 times tougher when subjected to indentation from the outer surface, coincident with the loading which would be applied by a predator tooth, as the microstructure restricts cracking. Previous fracture toughness measurements performed on the bone region of the scale by Yang *et al.* [13] used notched beams to yield fracture toughness crack-resistance curves in three orientations. The toughness rises to $K_j = 6$ MPa $m^{1/2}$ as the crack grows, depending on orientation. Our toughness values of 0.8–2.8 MPa $m^{1/2}$ represent the early stages of crack growth where extrinsic toughening mechanisms start to become operational, and are consistent with the first part of the fracture toughness crack-resistance curves by Yang *et al.* [13].

Three-point bending tests were performed on specimens of the scale that include both ganoine and bone regions. Two loading directions were used, and results are shown in figure 9. Significant differences in response between the two directions exist: when the scale is bent with the ganoine in tension, the maximum flexural stress is 73 ± 6 MPa. The brittle mineral is not effective at supporting substantial tensile loads and failure originates in the ganoine. In contrast, the ganoine has a high compressive strength and, when loaded in compression, the maximum flexural stress increases to 160 ± 20 MPa. This coincides with the functional requirements of the gar scale and many other armours, where attack and pressures occur from the exterior and a hard outer surface exists to prevent penetration, but a more compliant foundation capable of supporting tensile loads is required. In the gar scales, the ganoine is in compression and the bone provides the required tensile strength.

Penetration tests were performed using a steel indenter with a 300 µm tip radius on individual scales with and without the ganoine layer, in order to determine its contribution. The ganoine layer was removed just beyond the interface of the two layers by careful polishing to prevent the introduction of damage. The results, shown in figure 10*a*, are

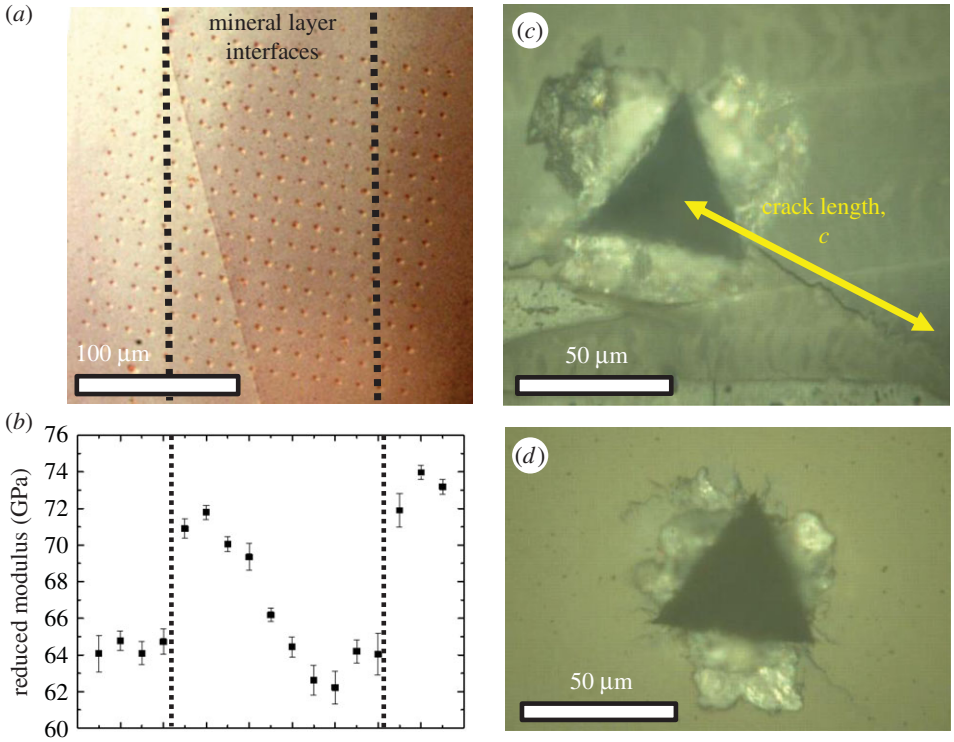

Figure 8. Nanoindentation of ganoine normal and parallel to the scale surface. (*a*,*b*) The variation of modulus corresponds to the layers of ganoine. (*c*) In the transverse direction of the scale, a high load indent causes cracks to grow; crack semi-length, *c*, is marked. (*d*) In the normal direction to the scale, smaller cracks caused by a high load indent correspond to an increased toughness. (Online version in colour.)

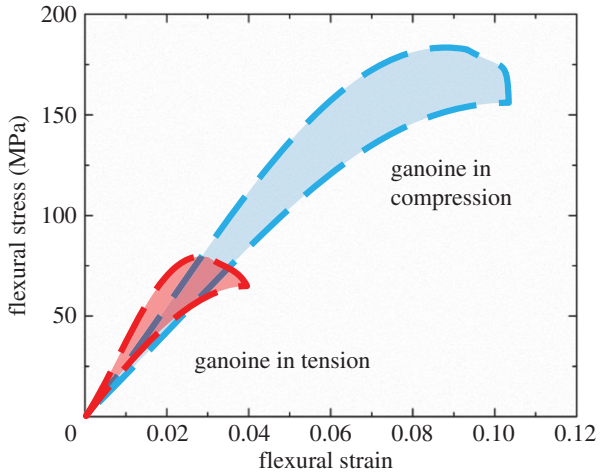

Figure 9. Three-point bending of scale with ganoine and bony layers along two opposite directions. Bending tests produce tension on the convex face, and compression on the concave face. When the ganoine side is subjected to compression, higher flexural stresses and strains are achievable. This is due to the ganoine's compressive strength, and the bone's ability to resist high strains. The ganoine's weakness in tension decreases the flexural strength. (Online version in colour.)

surprising. The presence of ganoine against a steel indenter produces a slight decrease in the maximum force. In each case, the force to failure still remains sufficiently high to defeat predators as over 1500 N is required to cause failure. For comparison, large alligators may have a bite force of up to 10 kN, which is distributed among the approximately 80 teeth in the alligator's mouth [10]. It is difficult to evaluate the force per tooth because this depends on the relative size of fish and alligator mouth. We assume, to a first approximation, that one-third of the teeth are in contact. This gives an average force per tooth of up to 375 N. One possible explanation for this behaviour is that the localized penetration resistance decreases slightly with the ganoine layer but the flexure strength increases.

An additional penetration test performed with an alligator tooth is shown in figure 10*b*, which results in the failure of the tooth at 500 N. The cracking of the alligator tooth is induced by the hardness of the ganoine layer, which prevents deformation and a distribution of the load across the alligator tooth. This shows that, with the ganoine layer, the gar scale is sufficiently strong to withstand local loads due to alligator bite force. Additionally, the hardness of ganoine may play a role in inducing the failure of teeth.

The sequence of images in figure 10*c* shows an array of scales deformed to accommodate the movement caused by the pressure on a central scale. A compliant foundation mimicking the flesh of the animal was used. The alligator tooth is embedded in the tip of a threaded rod, and pressure is initiated at (i). When the force reaches 500 N, the alligator tooth fractures (ii). Upon removal of the force (iii), the array of scales returns to the flat and undeformed state. Through linkage with adjacent scales, the load is distributed from the point of application, reducing pressure and damage to the underlying soft tissues. Figure 10*d* indicates how the pressure from indentation leads to flexural loadings, and shows how the ganoine may be beneficial in this regard.

5. Failure aversion strategies in the gar scale

There are three regions in the single gar scale where key failure aversion features occur: (i) in the ganoine, where cracks initiate during predatory attack, (ii) at the interface between

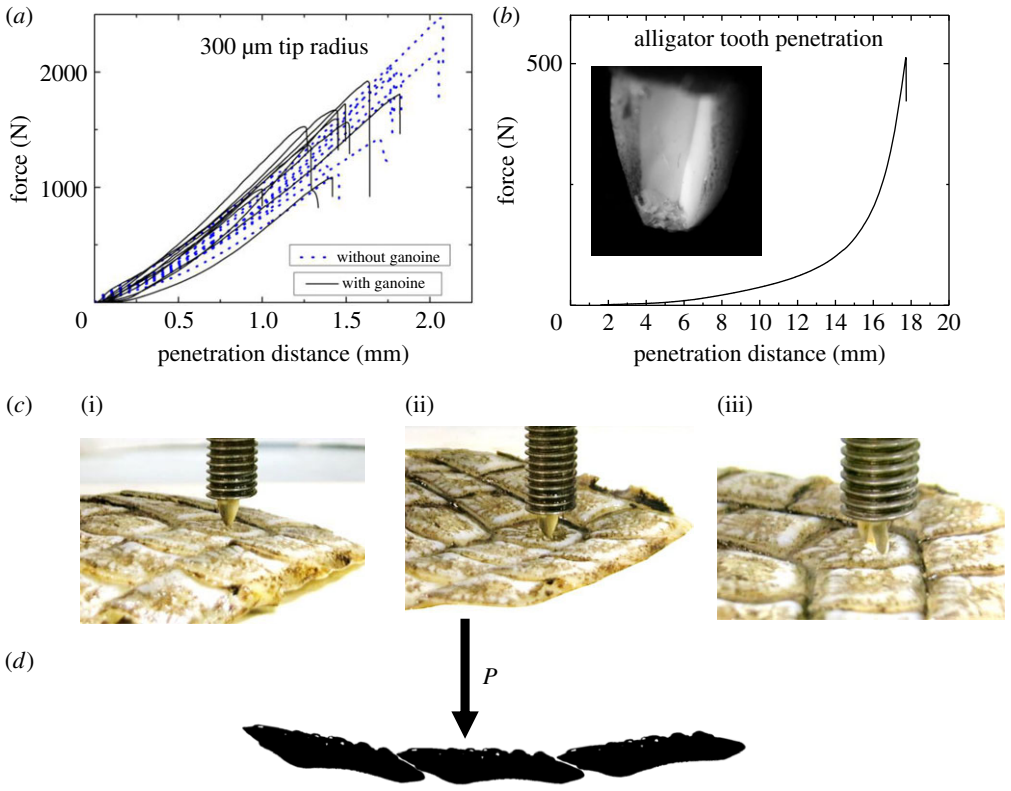

Figure 10. Penetration of an individual scale by a steel penetrator and an alligator tooth. (*a*) Sections of scale both with and without the ganoine layer are indented by a steel tip. Scales without ganoine frequently experienced additional penetration, compaction and higher failure forces. By contrast, scales with the ganoine layer showed not only a reduced penetration at any force but also slightly reduced failure loads. (*b*) Load versus penetration of gar scale array by a young alligator tooth with a tip radius of 240 µm. Foam beneath the array simulates flesh. Tooth failure occurs at 500 N, which is significantly less than what the scale is capable of withstanding, as illustrated in (*a*). (*c*) Sequence of scale penetration: (i) undeformed scales, (ii) scales conforming to the pressure of the tooth and (iii) tooth fails. (*d*) Schematic representation of cooperative motion of scales linked by connective tissue in response to load *P*. (Online version in colour.)

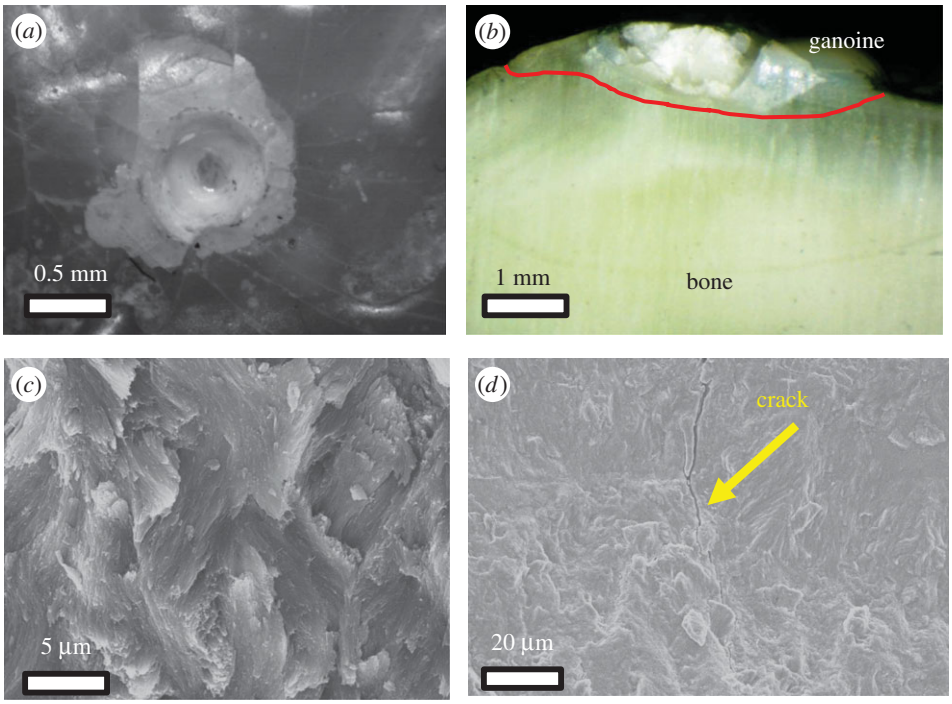

Figure 11. Toughening in the ganoine region. (*a*) Cracking of ganoine from penetration test loaded to 1000 N shows partial mineral failure, while bone remains intact. (*b*) Failure of ganoine during a compression test: failure is contained within the ganoine and does not propagate to bone. (*c*) Fracture surface of ganoine shows cross-plied mineral bundles that provide toughening. (*d*) A crack is arrested in the ganoine. (Online version in colour.)

the ganoine and bone, and (iii) in the bone region, which is the last stage of crack propagation, the fracture of which leads to complete failure of the scale.

Penetration tests into the ganoine reveal robust toughening features. Figure 11*a* is an indent caused by penetration of a steel indenter into the ganoine surface of the scale.

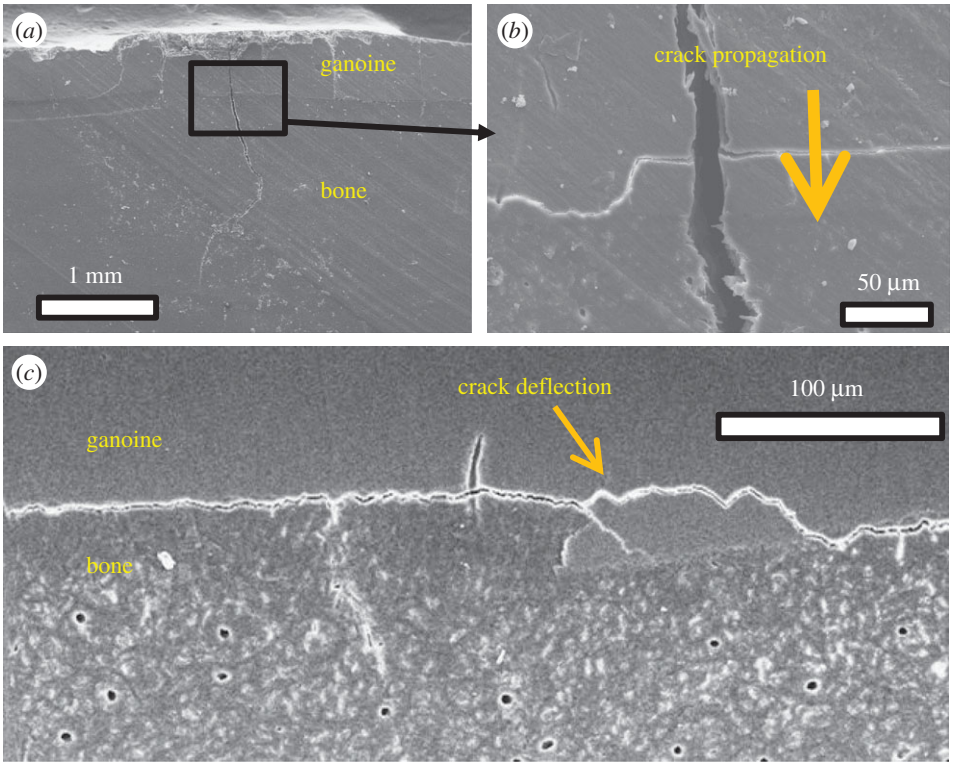

Figure 12. Interfacial toughening via crack deflection. (*a*) Large cracks penetrate through the ganoine and bone. (*b*) Magnified view of the interface in (*a*). Upon arrival at the ganoine–bone interface, cracks are deflected along the interface and, dependent on loading, may also continue into the bone. (*c*) Upon encountering the saw-tooth ridges in the interface, cracks are deflected into the ganoine where the toughening features within attempt to arrest the crack. (Online version in colour.)

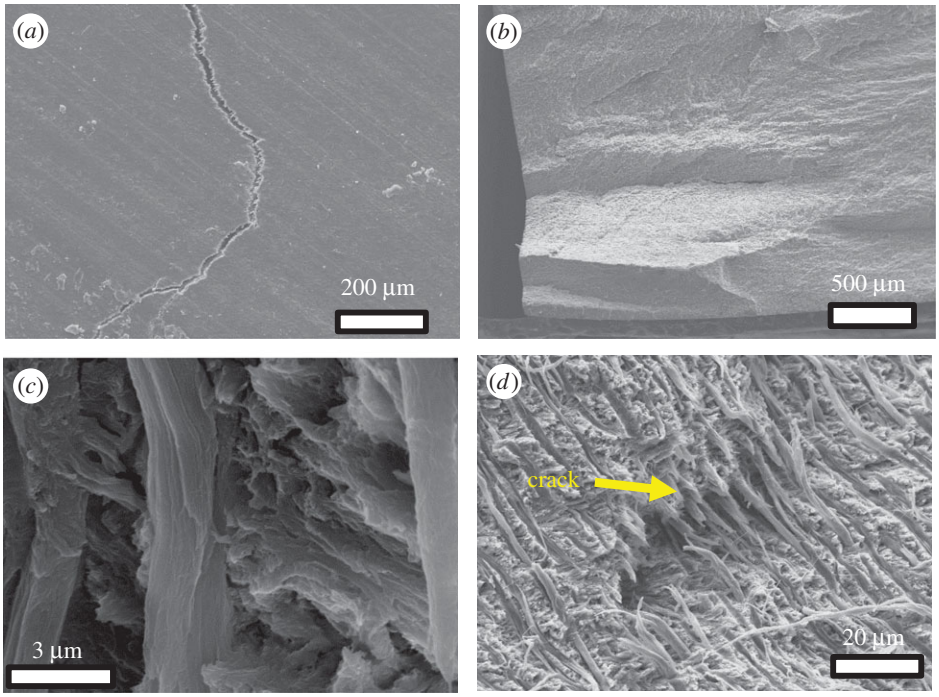

Figure 13. Toughening features of bony region: mineralized collagen fibrils. (*a*) The crack path as it penetrates through the bone layer is jagged. (*b*) The fracture surface of a hydrated scale. (*c*) A collagen fibril is shown with mineral crystals oriented across the fibril. This orientation is found throughout the scale. (*d*) Collagen fibrils stretch across a crack and prevent its propagation. (Online version in colour.)

After loading to 1000 N, damage to the ganoine is apparent as some crushing takes place, but the cracks do not propagate through the thickness of the scale. Cracking occurs directly beneath the indenter, and some cracks radiate out from the indenter but are contained within the ganoine layer. This is directly related to the fracture toughness, which is enhanced by the twisted cross-plied mineral, and a likelihood of multiple cracking within the ganoine, as observed in the conch shell [25]. Similarly, in a compression test of a portion of the scale with the ganoine layer intact (figure 11*b*), failure occurs in the ganoine layer but does not propagate to the interface with the bone layer. Close observation of the failure

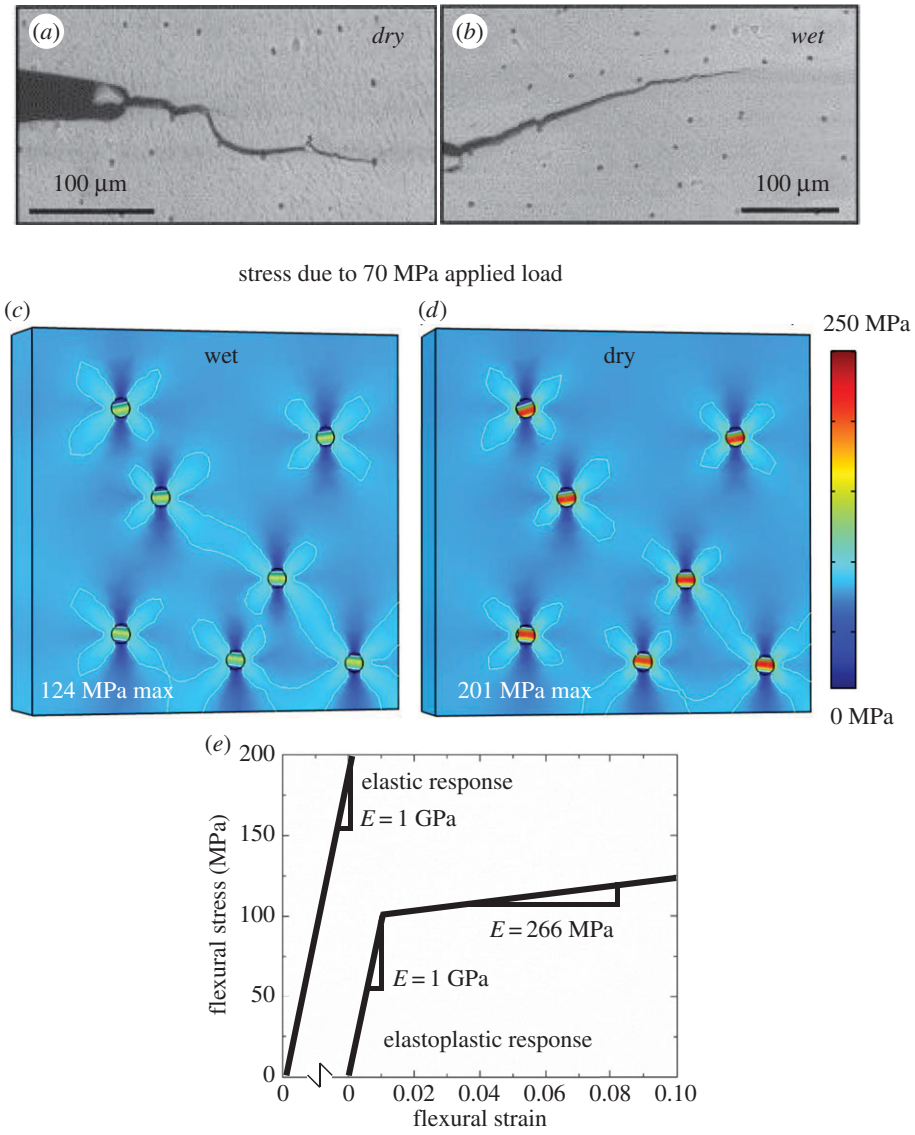

Figure 14. Toughening features of bony region: tubule effects. (*a*) A crack in a dry scale progresses by jumping from one tubule to the next. (*b*) A crack in a wet scale progresses without strong influence of the tubules. Adapted from Yang *et al*. [13]. (*c*,*d*) Simulations calculate stress in the presence of tubules when wet and dry. Stress concentrations around dry tubules correspond closely with three times the applied load, while stress concentrations around wet tubules are reduced by 38%. (*e*) The material responses applied for the elastic and elastoplastic responses. (Online version in colour.)

surface of ganoine (figure 11*c*) shows that, as cracks progress, they must twist and deflect since they follow the interfaces of cross-plied mineral bundles. This deflection toughens the mineral and inhibits the propagation of cracks, which are often arrested prior to penetrating the mineral layer. Figure 11*d* shows the containment of a crack in the ganoine layer.

The ganoine in the gar scale has the robust ability to arrest cracks, but this is not always sufficient. Figure 12*a* shows a crack, which originated during a three-point bending test and progressed through the ganoine into the bone. Material mismatch between two regions may cause crack deflection at the interface, based on Dundurs' parameters [26]. Imbeni *et al*. [27] present a solution for linear elastic materials based on the first Dundurs' parameter, $\alpha = (E_1 - E_2)/(E_1 + E_2)$, and the magnitude of material toughness on each side of the interface, G_1/G_2. For the case of a crack penetrating from ganoine towards bone, $\alpha = 0.71$ and $G_1/G_2 = 0.17$, indicating that cracks originating in the ganoine and arriving at the interface are well within the regime in which deflection is expected. Figure 12*b* shows a crack that arrives at the interface and is deflected along the border. The interface has a saw-tooth shape that directs the crack towards the mineral layer where it is either arrested by the robust toughening mechanisms within the ganoine or returns to the interface; this process may repeat and is shown in figure 12*c*.

With sufficient load, the bone will also crack. Energetically, it is expected that cracks propagate straight through the scale, along tubules (shown in figure 3), which create stress concentrations. Figure 13*a*,*b* shows an actual cracking path and overall jagged fracture surface, which results in a significant increase in the energy required to progress the crack. This meandering, possibly caused by the orientation of mineral crystals in the bone (shown in figure 13*c*), forces cracks to traverse highly mineralized fibrils with exceptional toughness, strength and elasticity. This closely aligns with the results by Yang *et al*. [13], which indicated that fracture toughness is enhanced for orientations where fibrils span the crack wake. Figure 13*d* shows one instance where collagen fibrils bridge a crack and aid in stopping propagation.

The role played by the tubules in the dry scales is well documented by Yang *et al*. [13] who note that in dry scales cracks are deflected between tubules, leading to an

enhanced fracture resistance through crack meandering. This causes the dry brittle material to have similar and sometimes superior properties to the wet material, where these toughening effects do not occur. These results are shown in figure 14*a*,*b*. Owing to the typically hydrated state of the gar scales, finite-element simulations were performed, in order to observe the effects of the tubule in wet and dry scales. The results, shown in figure 14*c*,*d*, confirm the high stress concentrations in the vicinity of tubules in the dry state. Elastoplastic (simulating the wet scale) and linear elastic (simulating the dry scale) responses applied to the material are shown in figure 14*e*. Owing to the linear elasticity of the dry material, the stress concentration around tubules closely corresponds with the relationship $\sigma_{max} = 3\sigma_{applied}$: $\sigma_{max} = 201$ MPa for $\sigma_{applied} = 70$ MPa. The stress distribution is inhomogeneous and high stresses at the edges of tubules induce failure. Crack tips tend to orient towards the direction perpendicular to the maximum normal stress, although in this case attraction to the intense stress around tubules leads to meandering. 'Wet' simulations incorporate the elastoplastic response of the material; this leads to a situation where $\sigma_{max} < 3\sigma_{applied}$: $\sigma_{max} = 124$ MPa for $\sigma_{applied} = 70$ MPa. The elastoplastic response reduces the stress intensity by 38%, while regions of high strain form around tubules (15% versus 11%), absorbing strain energy. These calculations explain the previous results by Yang *et al*. [13], confirming that the stress concentrations at the tubules direct the crack tip towards them and thus is a toughening mechanism. This does not occur in the wet scales, where simulations indicate that intrinsic toughening due to the plasticity of the bone operates in the vicinity of tubules. The reduction of stress intensity around tubules results in a more homogeneous distribution of stress. Therefore, an overall high value of strain is achieved prior to the material reaching failure, and an exceptional toughness as measured by the area beneath the tensile stress–strain curve in figure 7*a*.

6. Summary and conclusions

The goal of studying natural armour is to understand key features for potential incorporation into superior protection for personnel and equipment. Being in a hostile environment demands an effective armour capable of withstanding projectiles and impacts without inhibiting mobility. Tactical advantages are provided by advanced robotics, and armour which allows for flexibility is key to the protection of both human and machine.

This work extends the earlier contributions of our own group [12,13], which focused solely on microstructural features, and reveals design principles on the micro- and macroscales. These features are currently in the process of being incorporated into synthetic scale-inspired flexible designs: at the microscale, key features lead to the required material properties such as toughness and strength. At the macroscale, geometry provides the required coverage and flexibility while minimizing weaknesses. The following are the principal findings:

— The arrangement of scales in the quasi-cylindrical body of the gar makes an angle of $\gamma = 55^\circ$ with the longitudinal axis. Upon flexing, one side of the gar is stretched while the other is compressed. Both sliding and rotation, necessary to permit the length changes, are quantitatively expressed as a function of the flexing radius of the fish. Calculations show that the angle $\gamma = 55^\circ$ is a compromise between coverage area per tile and sliding/rotation on stretching.
— The scale, placed on a muscle simulant, was subjected to the increasing force of an alligator tooth. The scale resisted a bite force of 500 N, and the tooth broke. The radius of the tooth and maximum bite force depend on the mass and nature of the predator, but it is clear that the hard ganoine layer is effective in producing fracture of the tooth. Bending tests show that the flexural strength shows a considerable asymmetry; the orientation corresponding to attack (compressive force by an external load) is significantly enhanced.
— Toughening features exist in each layer of the scale. In the outer ganoine, twisted cross-plied mineral enhances fracture toughness and arrests cracks. The microstructural arrangement of the composite bone lengthens crack paths and uses the tough collagen fibrils. The saw-tooth interface between the two layers is designed to deflect and arrest cracks.

Data accessibility. Supporting data are available upon request from mameyers@ucsd.edu.

Authors' contributions. V.R.S. conducted most experiments; N.A.Y. and D.K. performed nanoindentation; M.A.M. directed the project. V.R.S. and M.A.M. drafted the manuscript. All authors gave final approval for publication.

Competing interests. We declare we have no competing interests.

Funding. The majority of this work was funded by the Multi-University Research Initiative grant no. AFOSR-FA9550-15-1-0009 from the Air Force Office of Scientific Research. μ-CT imaging performed at the National Center for Microscopy and Imaging Research at the University of California, San Diego was funded by National Institutes of Health grant P41GM103412 to Mark H. Ellisman.

Acknowledgements. We gratefully acknowledge Dianne and Gary Ulery for generously providing a supply of alligator gar scales. We thank Eric Bushong for assistance with recording of μ-CT data and Jerry Jung for assistance in the data reconstruction. Discussions with Prof. Joanna McKittrick, Prof. Robert Ritchie, Eric Hahn, Wen Yang, Tarah Sullivan and Bin Wang were helpful in the development of our ideas.

References

1. Wang B, Yang W, Sherman VR, Meyers MA. 2016 Pangolin armor: overlapping, structure, and mechanical properties of the keratinous scales. *Acta Biomater.* **16**, S1742–S7061. (doi:10.1016/j.actbio.2016.05.028)
2. Erdkamp P. 2011 *A companion to the Roman army*. Blackwell Companions to the Ancient World. Oxford, UK: Wiley-Blackwell.
3. Song J, Ortiz C, Boyce MC. 2011 Threat-protection mechanics of an armored fish. *J. Mech. Behav. Biomed. Mater.* **4**, 699–712. (doi:10.1016/j.jmbbm.2010.11.011)
4. Bigi A, Burghammer M, Falconi R, Koch MHJ, Panzavolta S, Riekel C. 2001 Twisted plywood pattern of collagen fibrils in teleost scales: an X-ray diffraction investigation. *J. Struct. Biol.* **136**, 137–143. (doi:10.1006/jsbi.2001.4426)
5. Giraud MM, Castanet J, Meunier FJ, Bouligand Y. 1978 The fibrous structure of coelacanth scales: a twisted 'plywood'. *Tissue Cell* **10**, 671–686. (doi:10.1016/0040-8166(78)90054-X)

6. Meyers MA, Chen PY, Lin AYM, Seki Y. 2008 Biological materials: structure and mechanical properties. *Prog. Mater. Sci*. **53**, 1–206. (doi:10.1016/j.pmatsci.2007.05.002)
7. Lin YS, Wei CT, Olevsky EA, Meyers MA. 2014 Mechanical properties and the laminate structure of *Arapaima gigas* scales. *J. Mech. Behav. Biomed. Mater*. **4**, 1145–1156. (doi:10.1016/j.jmbbm.2011.03.024)
8. Helfman GS, Collette BB, Facey DE. 2009 *The diversity of fishes—biology, evolution, and ecology*, 2nd edn. Oxford, UK: Wiley-Blackwell.
9. Bruet BJF, Song JH, Boyce MC, Ortiz C. 2008 Materials design principles of ancient fish armour. *Nat. Mater*. **7**, 748–756. (doi:10.1038/Nmat2231)
10. Sherman VR, Quan H, Yang W, Ritchie RO, Meyers MA. In press. A comparative study of piscine defense: the scales of *Arapaima gigas*, *Latimeria chalumnae* and *Atractosteus spatula*. *J. Mech. Behav. Biomed. Mater*. (doi:10.1016/j.jmbbm.2016.10.001)
11. Browning A, Ortiz C, Boyce MC. 2013 Mechanics of composite elasmoid fish scale assemblies and their bioinspired analogues. *J. Mech. Behav. Biomed. Mater*. **19**, 75–86. (doi:10.1016/j.jmbbm.2012.11.003)
12. Chen PY *et al*. 2012 Predation versus protection: fish teeth and scales evaluated by nanoindentation. *J. Mater. Res*. **27**, 100–112. (doi:10.1557/jmr.2011.332)
13. Yang W, Gludovatz B, Zimmermann EA, Bale HA, Ritchie RO, Meyers MA. 2013 Structure and fracture resistance of alligator gar (*Atractosteus spatula*) armored fish scales. *Acta Biomater*. **9**, 5876–5889. (doi:10.1016/j.actbio.2012.12.026)
14. Allison PG *et al*. 2013 Mechanical properties and structure of the biological multilayered material system, *Atractosteus spatula* scales. *Acta Biomater*. **9**, 5289–5296. (doi:10.1016/j.actbio.2012.11.005)
15. Daget J, Gayet M, Meunier FJ, Sire JY. 2001 Major discoveries on the dermal skeleton of fossil and recent polypteriforms: a review. *Fish Fish*. **2**, 113–124. (doi:10.1046/j.1467-2960.2001.00046.x)
16. Wulff G. 1901 On the question of speed of growth and dissolution of crystal surfaces. *Z. Krystallogr. Minera.* **34**, 449–530.
17. Buehler MJ. 2007 Molecular nanomechanics of nascent bone: fibrillar toughening by mineralization. *Nanotechnology* **18**, 295102. (doi:10.1088/0957-4484/18/29/295102)
18. Chen IH, Yang W, Meyers MA. 2015 Leatherback sea turtle shell: a tough and flexible biological design. *Acta Biomater*. **28**, 2–12. (doi:10.1016/j.actbio.2015.09.023)
19. Yang W, Chen IH, Gludovatz B, Zimmermann EA, Ritchie RO, Meyers MA. 2013 Natural flexible dermal armor. *Adv. Mater*. **25**, 31–48. (doi:10.1002/adma.201202713)
20. Meyers MA, Lin YS, Olevsky EA, Chen PY. 2012 Battle in the Amazon: arapaima versus piranha. *Adv. Eng. Mater*. **14**, B279–B288. (doi:10.1002/adem.201180027)
21. Evans AG, Charles EA. 1976 Fracture toughness determinations by indentation. *J. Am. Ceram. Soc*. **59**, 371–372. (doi:10.1111/j.1151-2916.1976.tb10991.x)
22. Lawn BR, Evans AG, Marshall DB. 1980 Elastic-plastic indentation damage in ceramics—the median-radial crack system. *J. Am. Ceram. Soc*. **63**, 574–581. (doi:10.1111/j.1151-2916.1980.tb10768.x)
23. Pharr GM. 1998 Measurement of mechanical properties by ultra-low load indentation. *Mater. Sci. Eng. A* **253**, 151–159. (doi:10.1016/S0921-5093(98)00724-2)
24. Hassan R, Caputo AA, Bunshah RF. 1981 Fracture toughness of human enamel. *J. Dent. Res*. **60**, 820–827. (doi:10.1177/00220345810600040901)
25. Kessler H, Ballarini R, Mullen RL, Kuhn LT, Heuer AH. 1996 A biomimetic example of brittle toughening. (1) Steady state multiple cracking. *Comput. Mater. Sci*. **5**, 157–166. (doi:10.1016/0927-0256(95)00067-4)
26. Dundurs J. 1969 Edge-bonded dissimilar orthogonal elastic wedges under normal and shear loading. *J. Appl. Mech*. **36**, 650–652. (doi:10.1115/1.3564739)
27. Imbeni V, Kruzic JJ, Marshall GW, Marshall SJ, Ritchie RO. 2005 The dentin–enamel junction and the fracture of human teeth. *Nat. Mater*. **4**, 229–232. (doi:10.1038/nmat1323)